Article

Autoencoder for parameter estimation and current-voltage curve simulation of perovskite solar cells

Check for updates

Oliver Zbinden[1,2], Ennio Luigi Comi[1], Evelyne Knapp[1] & Wolfgang Tress[1] ✉

In perovskite solar cells (PSCs), key quantities crucial for understanding physical processes, like electronic/ionic parameters, are difficult or impossible to measure directly. This study uses Autoencoders (AEs) to provide parameter values for different physical quantities of PSCs. The data set used for Machine Learning (ML) is simulated with a 1D drift-diffusion (DD) model, mimicking real-world devices. AEs are trained with the simulated data and, after learning, the encoder part of the AE is used for parameter estimation of measured PSCs. These estimates are retaken for new DD simulations that are compared to the measurements for validation, since the true device parameters are unknown. Furthermore, the decoder can be regarded as a device simulator restricted to the training data regime. The results show that AEs obtain device parameter estimates within seconds for the studied PSC devices. This procedure is applicable to gain a deeper understanding of device behaviour, for example, to study effects of degradation or different manufacturing processes.

Optimizing available technologies and developing new ways to offer cost-effective and clean energy solutions is vital to reduce CO_2 emissions and accelerate the transition to a sustainable society. Photovoltaics have been proven to provide a good solution. A new family of candidate materials, perovskites, is of particular interest. In only about a decade, the power conversion efficiency (PCE) of PSCs has increased from below 10%[1] to more than 26%, and even 34.6% in tandem configuration with silicon solar cells[2–4]. Due to their easy and inexpensive production, together with many favourable properties such as tunable band gap[5], good light absorption coefficient[6,7], and high defect tolerance[8,9], PSCs receive a lot of attention from the scientific community, but there are still several challenges to overcome. For example, device efficiency and stability improvements are often based on trial and error, where time and resources are expended without a guarantee of success. Furthermore, PSCs are still not fully understood because the interplay between the various layers making up the solar cell is complex, and some processes cannot be measured directly, or only with a large effort. These factors make it difficult to identify sources of under-performance, efficiency losses, or degradation of a device. Developing a deeper understanding of physical processes and device behaviour is crucial to advancing PSC technology to the next level.

Measuring current-voltage (J–V) curves is well established, and performed for almost every single device that is manufactured. In contrast, it can be challenging, or even impossible, to directly measure some specific physical parameters that influence the J–V curve and, therefore, overall performance. J–V curves already contain valuable information about a PSC, which is not directly accessible. To understand physical processes such as degradation better, or to find reasons for under-performance, it is important to use as much information about a device as possible. It is shown how ML can be used to extract such parameters from J–V curves. There are large databases[10,11] and substantial collections of individual research groups containing a plethora of information, including experimental J–V curves and other key figures. ML has already found many different applications in the field of PSCs, but most of the research focuses on discovering new materials[12,13], predicting material properties[14,15], or performance or degradation over time[16–18], which contributes to the improvement of existing devices, but does not necessarily lead to a deeper understanding from a physics perspective.

One possible way to make use of available J–V data is ML, for example, Autoencoders (AEs)[19–23] or variations of this family of algorithms. AEs take some n-dimensional input, transform it to the so-called latent space with a chosen dimension m, and try to reconstruct the input from these latent parameters.

In the field of PSCs, ML has been proven capable of inferring device parameters that influence the performance quantitatively[24]. This is one example that shows the enormous potential of how to use ML in this field and how the technology of PSCs can be further improved. Identifying the dominant recombination process[25] or the overall dominant performance-limiting effect[26] are some recent examples. For organic solar cells, ML has

[1]Institute of Computational Physics, Zurich University of Applied Sciences, Winterthur, Zurich, Switzerland. [2]Department of Mathematical Modeling and Machine Learning, University of Zurich, Switzerland, Zurich, Zurich, Switzerland. ✉e-mail: wolfgang.tress@zhaw.ch

Fig. 1 | Illustration of the AE with custom loss function. The encoder is not given the true parameters y, only x. The true parameters are only used in the loss function that calculates the difference between the true parameters y and the encoded latent space $y\prime$. The simulation results x are taken as encoder input, and to calculate the reconstruction loss. For the steady-state case, x are the illumination intensity-dependent J–V curves, and for the transient case, x are the scan speed-dependent J–V curves. Y are the respective material parameter sets that were varied in simulation.
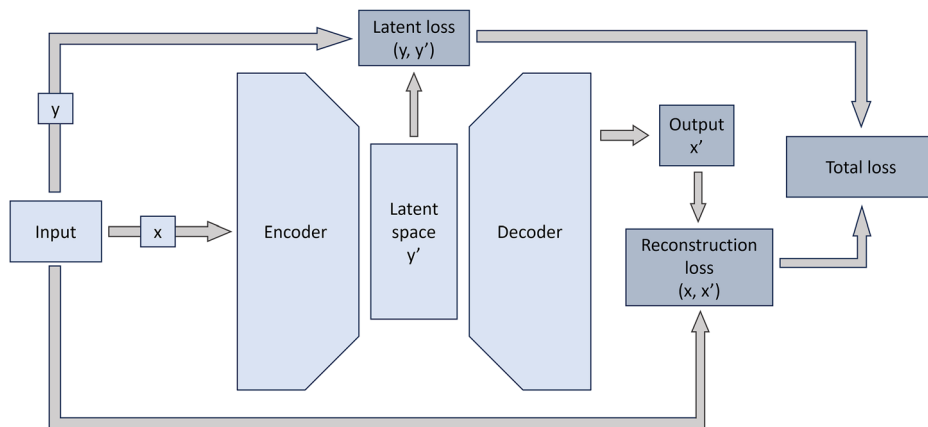

Table 1 | R^2 and $f_{0.2}$ (fraction of estimated parameter values with an absolute residual smaller than 0.2) as a quality measure

Param.	Steady-state		Transient	
	R^2	$f_{0.2}$	R^2	$f_{0.2}$
S	0.911	0.952	0.500	0.703
μ	0.980	0.990	0.984	0.993
τ	0.921	0.960	0.888	0.942
μ_{TiO_2}	0.721	0.829	0.351	0.666
ρ_{Ion}	0.996	1	0.859	0.941
μ_C	–	–	0.961	0.985
J	0.996	–	0.988	–

been used to extract material parameters[27], or to understand the influence of different fabrication protocols[28]. It has been shown how AEs can be used to optimize processing conditions in order to maximize the performance for different types of solar cells[29,30]. Several types of AEs are widely used in different scientific fields with remarkable results, for example, denoising AEs (DAEs)[22,31], variational AEs (VAEs)[32] for regression[33,34], or conditional VAEs (CVAEs) for fast prediction using stochastic feed-forward inference[35]. Compared to standard AEs, methods like VAEs use a probabilistic approach to model the latent space with a prior assumption for the parameter distribution and incorporate a regularization term in the loss function that allows continuous latent representations. The latent variables can further be forced to approximate some values by an additional constraint, as shown in different studies[36,37]. These CVAEs have an objective function with a conditional vector embedded, and therefore actively influence the loss function, which acts on updating the weights in the encoder and decoder.

Since the goal of this project is to estimate certain parameters from PSCs and to have a surrogate device simulator, AE-type neural networks (NNs) are of special interest. This study demonstrates how physical parameters can be estimated with the AE described in "Results", only based on measured J–V curves under different illumination intensities or scan speeds. With the correct choice of m and the chosen architecture of the AE (Fig. 1), the latent space is trained to match the physical quantities known from simulation, solely based on J–V curves as an input. As an example, PSCs from *Solaronix*[38] are examined, and the predictions from the AEs are verified with device simulation and measurements. The presented method offers many possible applications in research and industry. For example, it can be used to skip time-consuming parameter measurements in a first step, to quickly see the influence of different fabrication protocols during manufacturing devices, or in industrial fabrication, to screen large numbers of PSCs in a short amount of time and sort out bad devices. Importantly,

information about parameters that are not easily accessible improves the overall physical understanding of PSCs.

Results

Two different data sets are simulated and used to train different AEs, one for the steady-state case and one for the transient case. Steady-state means that the device is in electronic and ionic equilibrium at each applied voltage value during the J–V scan, namely that the mobile ions have settled for the measurement period. In contrast to steady-state, transient means that the device is not necessarily in equilibrium. The results obtained in transient simulations and measurements depend on different factors, such as scan speed and scanning direction. Transient measurements reveal details about some properties, for example, mobile ion densities and mobilities. For the steady-state case, in the bulk of the mesoporous perovskite-metal oxide layers, the varied parameters are electron and hole mobilities μ_e, μ_h, the effective Shockley–Read–Hall lifetime for electrons and holes τ_e, τ_h, and anion and cation densities $\rho_{A, C}$. Surface recombination velocities of electrons and holes S_e, S_h at the interface between TiO_2 and the mesoporous TiO_2-perovskite layer, and electron mobility μ_{TiO_2} in TiO_2 are varied as well. For the second case with transient simulations, cation mobility μ_C in the mesoporous perovskite-metal oxide layers comes on top of the other parameters.

ML model evaluation

The first obvious sanity checks are to compare the true simulation parameters with the latent parameters found by the encoder, as well as the simulated J–V curves with the AE output for the previously unseen test set. The reconstruction of the input J–V curves works rather well, according to the R^2 values for J in Table 1. Since this R^2 is only an average over all scan speeds of all J–V curves, it is more insightful to examine the voltage-resolved residuals for each scan speed individually (Supplementary Fig. 1). The residuals increase as the voltage increases for all scan speeds, because as voltage increases, the slope of a J–V curve usually increases. Peaks and valleys in these residuals are mainly caused by "bumps"[39], an ionic phenomenon that depends on scan speed and scanning direction. They were also measured for the studied devices (e.g. Supplementary Figs. 2 and 3g, h). Peaks represent predicted but not simulated bumps, and valleys represent simulated but not predicted bumps. This means that the decoder results are very similar compared to the DD simulation. More precisely, the estimated parameters lead to J–V curve predictions that are comparable to the initial simulation. Note that this does not necessarily lead to solutions that match the experimental measurements. Fig. 2 shows the estimated vs. true parameters for both models, steady-state and transient. Since the true range where the individual parameters were varied is known, one can see that in both cases, there are only very few outliers above the log-normalized maxima. The corresponding R^2 and $f_{0.2}$ are listed in Table 1, where $f_{0.2}$
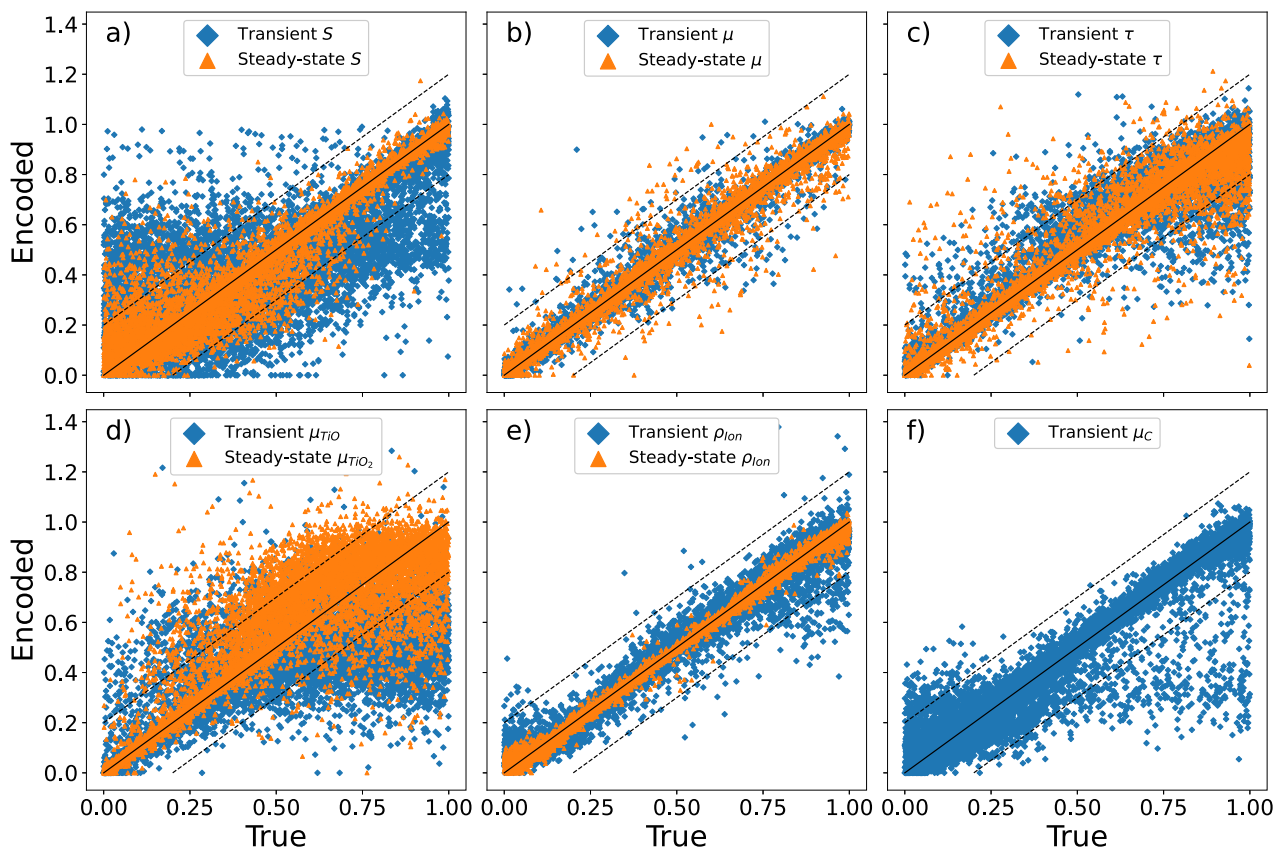
Fig. 2 | Log normalized parameter estimates for the test sets. Steady stare is represented as orange triangles, transient as blue diamonds. **a** S, **b** μ, **c** τ, **d** μ_{TiO_2}, and **e** ρ_{Ion} for both AE models, transient and stedy-state. **f** μ_C is only considered for the transient case. The dashed black lines show where the absolute value of the residual is 0.2, the solid black line indicates perfect agreement between true and encoded parameter values.

is the fraction of inliers within an absolute residual of 0.2, $f_{0.2} = \frac{|\{x_i||x_i^{pred} - x_i^{true}| < 0.2\}|}{N}$, with the corresponding parameter of the i-th simulated device x_i, the predicted and true values x_i^{pred}, x_i^{true}, correspondingly, and the total number of simulated devices N in the respective data set. For charge carrier mobilities μ and ion densities ρ_{Ion}, the results are excellent. These two parameters can be accurately determined (Fig. 2b, e), with R^2 close to 1. At least in the chosen parameter ranges (Table 3), changes of μ and ρ_{Ion} in simulation continuously influence the J–V curve, leading to different curves for different parameter values. The high accuracies indicate that the AE can detect the influence of these parameters on the J–V curves.

The other parameters (Fig. 2a, c, d, f) are more difficult for the AE to estimate, which is related to how they influence the J–V curves. Device simulation can help to visualise and understand the processes that lead to a mismatch in parameter estimation. Increasing one parameter systematically, and all other parameters still in a random way, shows that, for certain parameter regions, the J–V curves do not change anymore and become insensitive to these parameters. This indicates that the respective parameter ranges were chosen too broadly, which consequently leads to lower accuracies in prediction. This is shown in the residuals (Supplementary Fig. 4) for the transient case. The correlation matrix of the residuals in Supplementary Fig. 5 does not show substantial interdependencies, with values between 0.12 and −0.26 off the main diagonal. It does not mean that estimated parameters outside the simulated boundaries are unphysical, but one has to be cautious with these predictions. The surface recombination velocity S is difficult to predict if the values are small. At some point, it is so slow that the effect becomes negligible, approaching a limit that is close to the case where no interface recombination is present at all. The average time

an electron-hole pair exists before recombination is denoted by τ. When this is higher than the extraction time, which describes the average time it takes for charges to get out of the perovskite, the electron and hole have a high chance to get extracted from the perovskite layer and do not recombine anymore. Consequently, τ above some limit no longer influence the J–V curve. Of course this only holds as long as there is a current, so V_{OC} is unaffected. The influence of electron mobility in μ_{TiO_2} on the TiO₂ layer is more tricky because several effects are involved. The function of the TiO₂, the electron transport layer (ETL), is to select only electrons from the perovskite layer and transport them to the electrode. Higher μ_{TiO_2} is beneficial because then, charge extraction is more efficient and chances of recombination at the perovskite-ETL interface are lower. This results in higher short-circuit current J_{sc} and fill factor (FF). An efficient ETL can further lead to higher open-circuit voltage V_{oc}. Low mobilities in TiO₂ can cause charge accumulation at the perovskite-TiO₂ interface, leading to a more inhomogeneous electric field, deteriorating charge carrier transport in the device. Effects of ion mobilities μ_{Ion} can hardly be detected in steady-state, but possibly influence the transient J–V curves a lot. If the ionic mobilities are higher, a so-called hysteresis can be observed. This means that the J–V curves depend not only on the scan speed, but also on the scanning direction of a measurement.

To test if the latent parameter space can be further reduced, which can give an idea of how important the given parameters are for the AE, a physically intuitive approach is to define the conductivity σ. This is proportional to the product of mobility and charge density $\mu\rho$. Specifically, the cation conductivity $\sigma_C = \mu_C\rho_C$, calculated directly from the simulated data, is considered together with μ, S, τ, and μ_{TiO_2}. However, the accuracy of σ_C (Supplementary Fig. 6) is lower than μ_C and ρ_C, which indicates that the latent parameter space cannot be further reduced in the transient case without a negative influence on the latent parameter accuracy.
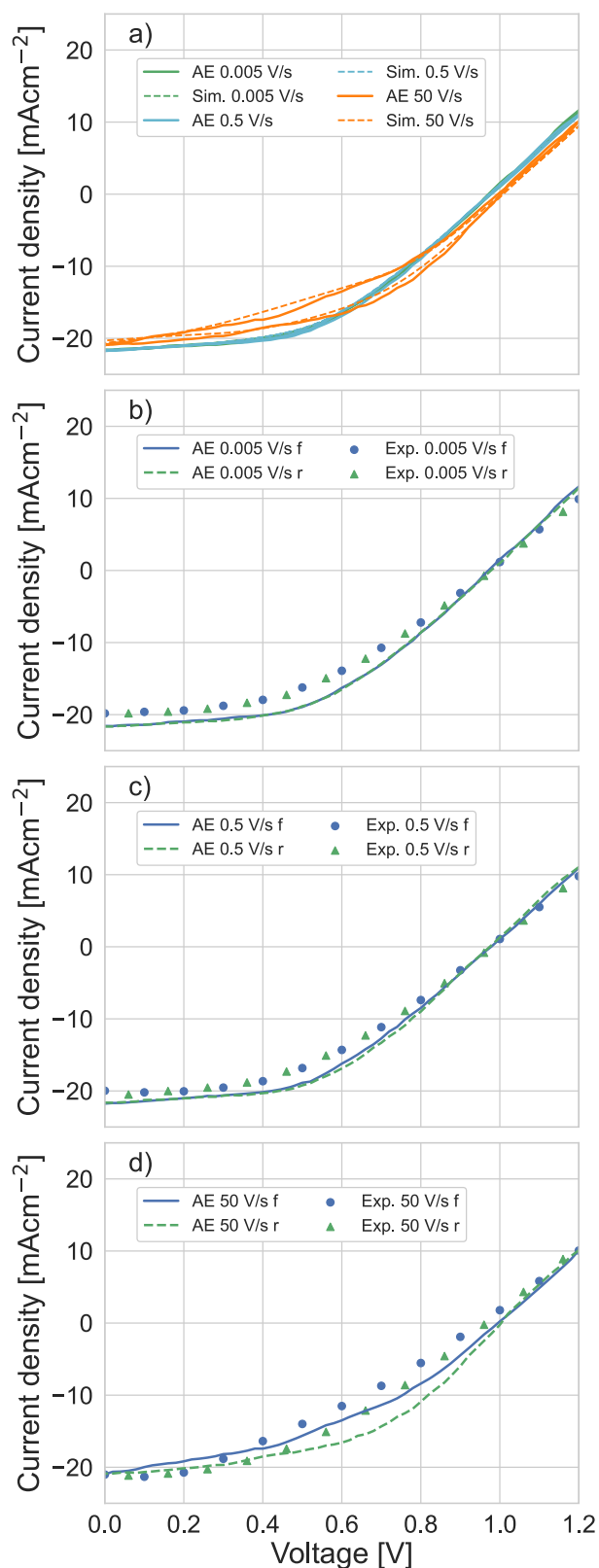
Fig. 3 | Comparison between the different results for one example, device A1.
a Decoder output (solid), and the re-simulations (dashed), based on the estimated
parameters, with the different scan speeds 0.005 V/s (green), 0.5 V/s (blue), and
50 V/s (orange). **b–d** Decoder output (blue solid lines forward scan, green dashed
lines reverse scan) and measurement (blue dots forward, green triangles reverse). For
better visibility, only half of the scan speeds are shown here. More data can be found
in Supplementary Fig. 7.

Application

Four devices from *Solaronix*[38] are measured and passed to the encoder for
regression. To prove the reliability of the presented method for parameter
estimation, the encoder estimates are used to re-simulate devices with these
parameters. The results are then compared to the performed measurements
and to the decoder output as well. Measurement and simulation must be
performed under the same conditions regarding the order of scan speed and
scanning direction described in "ML model evaluation" and "Application".
Additionally, the simulated illumination intensity and spectrum should
match the solar simulator used. The steady state is usually very challenging
to reach experimentally in a reasonable amount of time, which has also been
the case for the examined devices[40]. As a consequence, only the application
with transient measurements can be demonstrated. Figures 3 and Supple-
mentary Fig. 7 compare the measured transient currents, the AE output, and
the re-simulation for one of the devices.

In Fig. 3a, the AE results are compared to the results from re-simula-
tion, based on the estimated parameters. Since it can be assumed that the DD
model is accurate for a given parameter set, the resulting *J–V* curves are
supposed to be the true results for a specific parameter combination. The
decoder, given the same parameters as the DD model, being so close to the
true *J–V* curves, is a good surrogate model. DD simulation for one device
takes approximately 250 s–400 s, and the decoder needs 20 ms–30 ms,
which is four orders of magnitude faster. These times were measured on a
high-end notebook (CPU: Intel Core i9-11980HK@2.6GHz, RAM: 32GB,
GPU: NVIDIA RTX 3080 Laptop GPU 16GB); the ratio stays similar or
increases slightly when other hardware is used. Simulation time also
depends on the number of available CPU cores.

Overall, measurement and decoder output in Fig. 3b–d agree, but with
some mismatch. The currents are predicted slightly too low, but the overall
shape of the *J–V* curve is estimated well. This does not hold when there is
notable hysteresis, which is neither predicted correctly by the AE nor in re-
simulation. This difference is most likely caused by ionic-electronic effects in
the mesoporous layers that cannot be properly simulated in the DD model.

As a consequence of Fig. 3a, the re-simulation based on the estimated
parameters does not exactly match the real device. What can be done in such
a situation is to fit a DD model manually to the measured *J–V* curves. This fit
contains some sort of estimate about the parameters provided by the AE,
and it also allows for giving an impression of whether the DD model
describes the measured device or not. Because there are 12 *J–V* curves to fit,
this is a very time-consuming task and is therefore only done for one device
(A1) as an example. It turns out that changing two parameters slightly
already improves the agreement between experiment and simulation a lot
(Supplementary Fig. 8). μ_{TiO_2} was reduced from 4.74×10^{-5} cm^{2}V^{-1}s^{-1} to
the lower bound of the allowed range, 2.50×10^{-5} cm^{2}V^{-1}s^{-1}, and the
electron and hole recombination lifetimes τ were reduced from 16.49 ns to
10 ns. Based on the spread of parameter estimates in the test data in Fig. 2,
these new values are still reasonably close to the predictions.

The sources of the remaining deviations can be many. Uncertainties in
measurement, as well as in parameter estimation, are neglected. The device
model used for generating the training set is an approximation based on
available information, many physical parameters have to be given specific
values in simulation, even though they are not exactly known. There are also
restrictions in simulation, for example, mesoporous layers cannot be
simulated directly with a 1D DD model, or anions being considered static. A
comparison of Fig. 3a, b–d indicates that the estimated parameters lead to
results that agree with simulation, but the simulation with these parameters
does not reproduce the measurement as accurately. While the *J–V* predic-
tion/simulation and experiment are more consistent for the two devices B1
and B2, especially the FF is predicted/simulated higher than what was
measured in case of the devices A1 and A2. This implies that the device
model used was not as close to reality as intended, and that the model is
closer to the devices B1 and B2. The reason for this is that there are notable
differences in efficiency between the two batches (Discussion), and the
initial simulation focused on the better devices B1 and B2. Lastly, different

Table 2 | Parameter estimations for the four measured devices

Param.	A1	A2	B1	B2	Units
S	1.43	$1.57 \cdot 10^{-2}$	$4.17 \cdot 10^{-2}$	11.01	cms^{-1}
μ	1.88	3.28	20.21	8.45	$cm^2V^{-1}s^{-1}$
τ	16.49	29.53	36.09	41.51	ns
μ_{TiO_2}	$4.74 \cdot 10^{-5}$	$3.83 \cdot 10^{-5}$	$1.25 \cdot 10^{-4}$	$8.85 \cdot 10^{-5}$	$cm^2V^{-1}s^{-1}$
μ_C	$1.25 \cdot 10^{-10}$	$7.88 \cdot 10^{-8}$	$1.13 \cdot 10^{-7}$	$1.02 \cdot 10^{-7}$	$cm^2V^{-1}s^{-1}$
ρ_{Ion}	$1.01 \cdot 10^{17}$	$4.98 \cdot 10^{17}$	$1.41 \cdot 10^{17}$	$2.16 \cdot 10^{17}$	cm^{-3}

Table 3 | Literature-oriented parameter range for the different quantities, based on physically reasonable boundaries

Param.	Minimum	Maximum	Units
S	10^{-3}	100	cms^{-1}
μ	10^{-2}	10^3	$cm^2V^{-1}s^{-1}$
τ	1	10^4	ns
μ_{TiO_2}	$2.5 \cdot 10^{-5}$	1	$cm^2V^{-1}s^{-1}$
ρ_{Ion}	10^{14}	10^{20}	cm^{-3}
μ_C	10^{-15}	10^{-4}	$cm^2V^{-1}s^{-1}$

Cation mobilities μ_C were only varied in the transient case.

parameter combinations can lead to very similar, or even the same, $J–V$ curves due to possible correlations. Since the parameter predictions still lead to good results, the presented method has proven to deliver reasonable outputs that can be used to study PSCs. The estimated parameters for all the measured devices are listed in Table 2. The simulated results for the other devices, consistent with the device discussed here, are shown in Supplementary Figs. 2, 3, and 9. One parameter that can be measured qualitatively is μ_C. From Table 2, one expects that the cations are slower for the devices A1 and A2 compared to B1 and B2. The tendencies in Supplementary Fig. 10 are consistent with the cation mobilities extracted from the encoder, which again supports the reliability of the encoder as a parameter extractor.

Discussion

It has been shown that conditional AEs can be used for parameter extraction from $J–V$ curves, which is of high value for the perovskite research community. Comparison of measurement, ML results, and simulation shows that the predictions are accurate to a high degree. Information about parameters that can be obtained this way is important for in-detail device studies since this reveals qualitative information about physical quantities that are challenging to measure otherwise. The advantage of using a decoder as a device simulator is the short amount of computation time needed compared to standard DD models, once the training is completed. The drawback of the decoder is its limitation to the device architecture on which the training data are built. However, it must be considered that different parameter combinations can lead to very similar $J–V$ curves. Uncertainties in device measurement are neglected, and the used AE outputs are point estimates. It does not provide uncertainties, neither on the parameters nor on the $J–V$ curves. In future work, these points can be addressed, for example, with VAEs, including uncertainty estimates in the latent parameter space. The principle of parameter estimation for PSCs with AEs is generalizable, with new training data, to different device architectures and parameters as long as each parameter is able to influence a $J–V$ curve independently. The results help to better understand underlying parameters, which hopefully lead to more stable devices with higher efficiencies. The applications are not only restricted to research. Industry can profit from these results as well, as quality control in high throughput production, where in-detail analysis of every manufactured cell or solar panel is not feasible.

Methods
Device simulation
To prove the capability of AEs finding parameters from $J–V$ curves, carbon electrode-based mesoporous metal-oxide-perovskite devices[41,42] from *Solaronix* with an FTO/TiO$_2$/m-TiO$_2$-MAPI/m-ZrO$_2$-MAPI/Carbon device structure are simulated with the 1D DD simulator *Setfos*[43]. DD simulation models the movement of charges, such as electrons, holes, and ions, caused by drift and diffusion. The outputs of the simulations are electrical currents and charge carrier distributions in a device. First, a standard reference device is simulated, based on information about the different material layers (Supplementary Fig. 11 and Supplementary Table 1). This way, it is possible to match the parameters that are supposed to be fixed for devices under examination. Then the parameters that shall be determined are randomly varied within physically reasonable limits for

every simulated device. The parameters to be determined have been selected based on two criteria. Firstly, they can be relatively variable in a material, for example, due to degradation. Secondly, they are representative when studying different effects, such as effects related to charge transport vs. charge recombination in the bulk of the perovskite layers or at their surfaces, and ionic vs. electronic effects. With the randomness of different parameter values, it is guaranteed that the data set does not only resembles devices with average performance, but also better, and more importantly, worse-performing examples. The "bad" examples are of special importance since the AE has to be capable of detecting flaws in devices.

For simplicity, we set $\mu_e = \mu_h =: \mu$, $S_{e, top} = S_{h, top} =: S$, $\tau_e = \tau_h =: \tau$, and $\rho_A = \rho_C =: \rho_{Ion}$. The ranges of variation are listed in Table 3. In literature, most parameters are reported for pure perovskite, there is only little information for mesoporous perovskite-metal-oxide materials[41,44]. The parameter ranges are therefore wider than what is normally used. This wide range of varied parameters in Table 3 introduces a good amount of generalizability, with simulated $J–V$ curves covering the entire space from a hypothetical device that outperforms state-of-the-art samples with this architecture within physically reasonable boundaries, down to examples that are completely degraded. The Shockley-Queisser limit is still far away, in real-world devices and in simulation. The simulated data used for training can be extended to these limits once needed. The simulation approach allows to obtain a sufficiently large data set that covers a wide range of different parameter combinations. Steady-state simulations were performed under (0.1, 0.3, 0.5, 0.75, 1) sun illumination intensities, the transients at a constant illumination intensity of 1 sun, with scan speeds of (0.005, 0.05, 0.5, 5, 50, 100) V/s. In total, simulations for about 50′000 devices were performed for the steady-state and transient models, respectively, where in case of the transient simulations, scan speeds were performed in decreasing order. Simulation takes up to seven days, depending on steady-state or transient (simulations were performed on a cluster with two Intel Xeon Platinum 8164@2GHz CPUs, total 52 cores).

ML model description
In principle, different types of NNs could be suitable for the given task, but several reasons favor the conditional AE. A "normal" AE without the additional loss function acting on the latent space would be able to group latent parameters without constraints on their values. This has two disadvantages. First, the function that transforms the latent parameters from the encoded value to the true simulation values is not defined. Second, even if the latent space has the same dimension as the parameter space varied in simulation, the order does not have to be the same. With six parameters, there are 6! = 720 possible orders. The same disadvantages apply to the VAE. A CVAE would be a suitable method for the addressed problem, but for different models, it was not possible to reconstruct the $J–V$ curves, even though parameter estimation was only slightly worse than the conditional AE. A separate NN that takes the role of the encoder or decoder, respectively, works well, and the individual results are slightly better compared to the conditional AE. Training of the two models takes significantly more time compared to the conditional AE. This drawback outweighs the small gain in accuracy.

The encoder takes an input x, in this case the simulated currents, and encodes them into the so-called latent parameter space y. Since the AE is undercomplete, this forces the encoder to compress the input in a way that the most useful information is preserved in the latent space. The encoder consists of two convolutional and three dense layers, the decoder is mirror-symmetric to the encoder, where the convolutional layers are introduced to smoothen possible noise in experimental data. The latent parameters are not only the input of the decoder, which is reconstructed into currents, but also a separate output that reveals information about the physical parameters. The simulated J–V curves are interpolated, each scan speed forward and backward 0 V-1.2 V-0 V in steps of 0.02 V, and normalized with the global minimum and maximum. All scan speeds for one simulated device are collected in a 1D array with a length of 732. This provides a fixed length of the input, which is needed for the AE. Additionally, this has the benefit that only the current is needed as an input, since the values for the voltage are always the same. Each varied physical parameter is log-normalized separately. After normalization, the data sets are split into parts of 70:15:15 for training, validation, and test sets. 10-fold cross-validation with a fixed seed was performed for the two AE models in both cases, where one fold took up to 8 h on a NVIDIA Tesla V100 32GB GPU.

In normal AEs the latent parameter space is not controlled, only its dimension is defined. The AE is therefore forced to decide how the input data should be compressed. It compares the input data with the output, using a suitable loss function, such as mean squared error (MSE) or mean absolute error (MAE). The latent parameters are not considered in the loss function because the AE is only given the dimension of the latent space, but not the true parameter values. This is because usually, the objective of such an AE is to compress the input efficiently, with the latent space's shape as the only requirement. A standard AE with additional conditions on the latent space, as depicted in Fig. 1. As used here, it should work like a CVAE. The total loss does not only consist of a measure that compares encoder input to decoder output, but also the latent space/encoder output and the true (simulated) parameters y. This approach[29] is interesting because the encoder and decoder parts of the trained AE can be used for different tasks independently. As already mentioned, the encoder part is capable of predicting several device and material parameters that are of interest for the perovskite community, conveniently based on J–V curves only. Secondly, the decoder is a very fast device simulator, since especially transient simulations are time-consuming. Based on the trained simulations, the decoder can generate a set of transient J–V curves for a desired parameter combination within seconds.

Device measurement

For the experimental part, J–V characteristics of four encapsulated mesoporous PSCs were measured. Two devices (B1, B2) were from a batch produced in 2023 that are well functional with PCEs of approximately 11% and two devices (A1, A2) that were produced in 2024 show lower FFs and consequently compromised PCEs of approximately 9%. The J–V characteristics have been measured under 1000 W/m^2 (1 sun) illumination with the multifunctional characterization platform *Paios* from Fluxim AG[45] with scan rates of (0.005, 0.05, 0.5, 5, 50, 100) V/s. The measurements have been taken with a measurement routine containing concatenated ramps. The scan speeds were conducted in descending order and in forward and reverse direction between −0.2 and 1.4 V, mimicking the simulation conditions. The 1 sun illumination has been provided with a class ABB AM1.5G solar simulator (LCS-100, 94011A, ORIEL, USA) that has been calibrated with a reference silicon solar cell (RS-ID-2, FHG-ISE).

The normalized transient electroluminescence (EL, Supplementary Fig. 9) signal has been extracted from images taken with a Basler a2A4504-18 μmPRO camera with a monochrome Sony IMX541 CMOS sensor that is incorporated in an in-house built measurement tool. A constant potential of 1.2 V has been applied to the devices with a National Instrument (NI) source measure unit (SMU) (PXIe-4138) for 300 s. Images were taken every 10 s with 10 s exposure time, resulting in a total of 30 images per device.

References

1. Kim, H.-S. et al. Lead Iodide perovskite sensitized all-solid-state submicron thin film mesoscopic solar cell with efficiency exceeding 9%. *Sci. Rep.* **2**, 591 (2012).
2. NREL. Best research-cell efficiency chart plotted by the National Renewable Energy Laboratory. https://www.nrel.gov/pv/interactive-cell-efficiency.html (2025).
3. Green, M. A. et al. Solar cell efficiency tables (version 64). *Prog. Photovolt. Res. Appl.* **32**, 425–441 (2024).
4. LONGi. 34.6%! Record-breaker LONGi once again sets a new world efficiency for silicon-perovskite tandem solar cells. https://www.longi.com/en/news/.
5. Zhang, Z., Wang, M., Ren, L. & Jin, K. Tunability of band gap and photoluminescence in CH3NH3PbI3 films by anodized aluminum oxide templates. *Sci. Rep.* **7**, 1918 (2017).
6. De Wolf, S. et al. Organometallic halide perovskites: sharp optical absorption edge and its relation to photovoltaic performance. *J. Phys. Chem. Lett.* **5**, 1035–1039 (2014).
7. Kato, M. et al. Universal rules for visible-light absorption in hybrid perovskite materials. *J. Appl. Phys.* **121**, 115501 (2017).
8. Ceratti, D. R. et al. Self-healing inside apbbr3 halide perovskite crystals. *Adv. Mater.* **30**, 1706273 (2018).
9. Steirer, K. X. et al. Defect tolerance in methylammonium lead triiodide perovskite. *ACS Energy Lett.* **1**, 360–366 (2016).
10. Jacobsson, T. J. et al. An open-access database and analysis tool for perovskite solar cells based on the FAIR data principles. *Nat. Energy* **7**, 107–115 (2022).
11. Beard, E. J. & Cole, J. M. Perovskite- and dye-sensitized solar-cell device databases auto-generated using chemdataextractor. *Sci. Data* **9**, 329 (2022).
12. Li, X. et al. Computational screening of new perovskite materials using transfer learning and deep learning. *Appl. Sci.* **9**. https://www.mdpi.com/2076-3417/9/24/5510 (2019).
13. Lu, S. et al. Accelerated discovery of stable lead-free hybrid organic-inorganic perovskites via machine learning. *Nat. Commun.* **9**, 3405 (2018).
14. Pilania, G. et al. Machine learning bandgaps of double perovskites. *Sci. Rep.* **6**, 19375 (2016).
15. Li, J., Pradhan, B., Gaur, S. & Thomas, J. Predictions and strategies learned from machine learning to develop high-performing perovskite solar cells. *Adv. Energy Mater.* **9**, 1901891 (2019).
16. Srivastava, M., Howard, J. M., Gong, T., Rebello Sousa Dias, M. & Leite, M. S. Machine learning roadmap for perovskite photovoltaics. *J. Phys. Chem. Lett.* **12**, 7866–7877 (2021).
17. Howard, J. M., Tennyson, E. M., Neves, B. R. & Leite, M. S. Machine learning for perovskites' reap-rest-recovery cycle. *Joule* **3**, 325–337 (2019).
18. Stoddard, R. J. et al. Forecasting the decay of hybrid perovskite performance using optical transmittance or reflected dark-field imaging. *ACS Energy Lett.* **5**, 946–954 (2020).
19. Fogelman-Soulié, F. & Le Cun, Y. Modèles connexionnistes de l'apprentissage. *Intellectica* **2**, 114–143 (1987).

20. Ballard, D. H. Modular learning in neural networks. In *Proc. Sixth National Conference on Artificial Intelligence*, Vol. 1, 279–284 (IEEE, 1987).

21. Kramer, M. A. Nonlinear principal component analysis using autoassociative neural networks. *AIChE J.* **37**, 233–243 (1991).

22. Kramer, M. Autoassociative neural networks. *Comput. Chem. Eng.* **16**, 313–328 (1992).

23. Hinton, G. E. & Zemel, R. Autoencoders, minimum description length and helmholtz free energy. In *Advances in Neural Information Processing Systems* (eds Cowan, J., Tesauro, G. & Alspector, J.) vol. 6 (Morgan-Kaufmann, 1993).

24. Battaglia, M. et al. Deep ensemble inverse model for image-based estimation of solar cell parameters. *APL Mach. Learn.* **1**, 036108 (2023).

25. Le Corre, V. M., Sherkar, T. S., Koopmans, M. & Koster, L. J. A. Identification of the dominant recombination process for perovskite solar cells based on machine learning. *Cell Rep. Phys. Sci.* **2**, 100346 (2021).

26. Zbinden, O., Knapp, E. & Tress, W. Identifying performance limiting parameters in perovskite solar cells using machine learning. *Sol. RRL* **8**, 2300999 (2024).

27. Knapp, E., Battaglia, M., Stadelmann, T., Jenatsch, S. & Ruhstaller, B. Xgboost trained on synthetic data to extract material parameters of organic semiconductors. In *Proc. 8th Swiss Conference on Data Science (SDS)*, 46−51 (IEEE, 2021).

28. Majeed, N. et al. Using deep machine learning to understand the physical performance bottlenecks in novel thin-film solar cells. *Adv. Funct. Mater.* **30**, 1907259 (2020).

29. Ren, Z. et al. Physics-guided characterization and optimization of solar cells using surrogate machine learning model. In *Proc. IEEE 46th Photovoltaic Specialists Conference (PVSC)*, 3054–3058 (IEEE, 2019).

30. Ren, Z. et al. Embedding physics domain knowledge into a Bayesian network enables layer-by-layer process innovation for photovoltaics. *npj Comput Mater* **6**, 9 (2020).

31. Vincent, P., Larochelle, H., Lajoie, I., Bengio, Y. & Manzagol, P.-A. Stacked denoising autoencoders: learning useful representations in a deep network with a local denoising criterion. *J. Mach. Learn. Res.* **11**, 3371–3408 (2010).

32. Kingma, D. P. & Welling, M. Auto-encoding variational bayes. arXiv preprint arXiv:1312.6114 (2013).

33. Yoo, Y., Yun, S., Chang, H. J., Demiris, Y. & Choi, J. Y. Variational autoencoded regression: high dimensional regression of visual data on complex manifold. https://arxiv.org/abs/1908.04015 (2019).

34. Zhao, Q., Adeli, E., Honnorat, N., Leng, T. & Pohl, K. M. Variational autoencoder for regression: application to brain aging analysis. http://arxiv.org/abs/1904.05948 (2019).

35. Sohn, K., Lee, H. & Yan, X. Learning structured output representation using deep conditional generative models. In *Advances in Neural Information Processing Systems* (eds Cortes, C., Lawrence, N., Lee, D., Sugiyama, M. & Garnett, R.) vol. 28 (Curran Associates, Inc., 2015).

36. Lim, J., Ryu, S., Kim, J. W. & Kim, W. Y. Molecular generative model based on conditional variational autoencoder for de novo molecular design. *J. Cheminform.* **10**, 31 (2018).

37. Gille, C., Guyard, F. & Barlaud, M. Semi-supervised classification using a supervised autoencoder for biomedical applications https://doi.org/10.48550/arXiv.2208.10315 (2022).

38. Solaronix, S. A. https://www.solaronix.com/ (2024).

39. De Moor, G. et al. Understanding the anomalous J-V curves in carbon-based perovskite solar cells as a structural transition induced by ion diffusion. *Sol. RRL* **8**, 2300998 (2024).

40. Torre Cachafeiro, M. A. et al. Ion migration in mesoscopic perovskite solar cells: effects on electroluminescence, open circuit voltage, and photovoltaic quantum efficiency. *Adv. Energy Mater.* 2403850. https://onlinelibrary.wiley.com/doi/abs/10.1002/aenm.202403850 (2024).

41. Kerremans, R. et al. On the electro-optics of carbon stack perovskite solar cells. *Sol. RRL* **4**, 1900221 (2020).

42. Bogachuk, D. et al. Comparison of highly conductive natural and synthetic graphites for electrodes in perovskite solar cells. *Carbon* **178**, 10–18 (2021).

43. Fluxim, A. G. Semiconductor Simulator (SETFOS). https://www.fluxim.com/setfos-intro (2024).

44. Neukom, M. T. et al. Consistent device simulation model describing perovskite solar cells in steady-state, transient, and frequency domain. *ACS Appl. Mater. Interfaces* **11**, 23320–23328 (2019).

45. Fluxim, A.G. Electrical and optical characterization of LEDs and solar cells (PAIOS). https://www.fluxim.com/paios (2024).

Acknowledgements

Author contributions
O.Z. and E.K.: Conceptualization, O.Z. and E.C.: Simulation, writing original draft, O.Z.: Coding, data curation, analysis, figures, E.C.: Experimental measurements, O.Z., E.K., and W.T.: Writing—review and editing, E.K. and W.T.: supervision, W.T.: project administration, funding acquisition. All authors reviewed the manuscript.

Competing interests
The authors declare no competing interests.

Additional information
Supplementary information The online version contains supplementary material available at https://doi.org/10.1038/s41524-025-01875-0.

Correspondence and requests for materials should be addressed to Wolfgang Tress.

Reprints and permissions information is available at http://www.nature.com/reprints

Publisher's note Springer Nature remains neutral with regard to jurisdictional claims in published maps and institutional affiliations.